**Biogeosciences
Discussions**

High-resolution interpolar difference of atmospheric methane around the Last Glacial Maximum

M. Baumgartner[1,2], A. Schilt[1,2], O. Eicher[1,2], J. Schmitt[1,2], J. Schwander[1,2], R. Spahni[1,2], H. Fischer[1,2], and T. F. Stocker[1,2]

[1]Climate and Environmental Physics, Physics Institute, University of Bern, Sidlerstrasse 5, 3012 Bern, Switzerland
[2]Oeschger Centre for Climate Change Research, University of Bern, 3012 Bern, Switzerland

Correspondence to: M. Baumgartner (baumgartner@climate.unibe.ch)

Title Page

Abstract	Introduction
Conclusions	References
Tables	Figures

Back | Close

Full Screen / Esc

Printer-friendly Version

Interactive Discussion

Full Screen / Esc

Printer-friendly Version

Interactive Discussion

Abstract

Reconstructions of past atmospheric methane concentrations are available from ice cores from both, Greenland and Antarctica. The difference observed between the two polar methane concentration levels is a valuable additional parameter which al-
5 lows to constrain the geographical location of the responsible methane sources. Here we present new high-resolution methane records from the North Greenland Ice Core Project (NGRIP) and the European Project for Ice Coring in Antarctica (EPICA) Dronning Maud Land (EDML) ice cores covering Termination 1, the Last Glacial Maximum, and parts of the last glacial back to 32 000 years before present. Due to the high-
10 resolution records the synchronisation between the ice cores from NGRIP and EDML is considerably improved and the interpolar concentration difference of methane is determined with unprecedented precision and temporal resolution. Relative to the mean methane concentration, we find a rather stable positive interpolar difference throughout the record with its minimum value of 3.7 ± 0.7 % between 21 900–21 200 years
15 before present, which is higher than previously estimated in this interval close to the Last Glacial Maximum. This implies that Northern Hemisphere boreal wetland sources were never completely shut off during the peak glacial. Starting at 21 000 years before present, i.e. several millenia prior to the transition into the Holocene, the relative interpolar difference becomes even more positive and stays at a fairly stable
20 level of 6.5 ± 0.8 % during Termination 1. We hypothesise that the anti-correlation observed in the monsoon records from the Northern and Southern Hemispheres induces a methane source redistribution within lower latitudes, which could explain parts of the variations in the interpolar difference.

1 Introduction

25 Methane (CH_4) is a trace gas with a global mean atmospheric concentration of about 1800 parts per billion by volume (ppbv) today and contributed to the greenhouse effect

with a radiative forcing (relative to 1750 AD) of $0.5\,\mathrm{W\,m^{-2}}$ in 2010 (Dlugokencky et al., 2011). The higher CH_4 emissions in the Northern Hemisphere compared to the Southern Hemisphere induce an interpolar concentration difference (*IPD*) which today is (under the anthropogenic influence) about 127 ppbv (7 %) averaged over the year 2010

5 (Dlugokencky et al., 2011). Knowledge of the past latitudinal source distribution is valuable to understand the biogeochemical and climatic changes occuring in glacials, interglacials, and during rapid climate changes such as Dansgaard/Oeschger (DO) events. As the main control of the past *IPD* we consider the latitudinal distribution of emissions from boreal and tropical wetlands, which contribute 60–80 % to the total natural source

10 today (Denman et al., 2007). A recent modelling study (Weber et al., 2010) estimates a 4–18 % smaller wetland area and a 35–42 % lower wetland CH_4 flux during the Last Glacial Maximum (LGM) compared to the preindustrial Holocene. Wetland CH_4 productivity depends on temperature, precipitation, and availability of organic material, where recent satellite data show that temperature is the more critical factor in high north-

15 ern latitudes and water table depth more dominant in the tropics (Bloom et al., 2010). Thus changes in the latitudinal distribution of temperature and consequent changes in the latitudinal distribution of precipitation might have regulated changes in the wetland source distribution in the past. The former one depends on insolation and on the heat transport across the equator connected to the Atlantic Meridional Overturing Cir-

20 culation (AMOC), which leads to a bipolar temperature seesaw (Stocker and Johnsen, 2003).

The atmospheric concentration of CH_4 is not only influenced by the sources, but also by the sinks. The major sink is the oxidation in the troposphere by the hydroxyl radical (OH), which has its maximum abundance in the tropics (Hein et al., 1997). CH_4

25 has a mean atmospheric lifetime of 8.7 ± 1.3 years today (Denman et al., 2007). The influence on the atmospheric lifetime of CH_4 of sink competitors like Biogenic Volatile Organic Compounds (BVOC) is still debated. While Kaplan et al. (2006) invoke major changes in the atmospheric lifetime due to large changes in the BVOC emissions over Termination 1, Levine et al. (2011) find that the effect of BVOC is negligible.

Ice cores from Greenland and Antarctica allow us to reconstruct past atmospheric CH_4 variations and hence to constrain the latitudinal source distribution by the knowledge of the *IPD* (Brook et al., 2000; Chappellaz et al., 1997; Dällenbach et al., 2000). In this study, we measure the CH_4 concentration along the NGRIP (Greenland) and EDML (Antarctica) ice cores. In a two-box model simulation, the measured concentrations are used as inputs to estimate the source strengths in both the Northern and Southern Hemisphere. Finally, we discuss the processes, which might have caused the observed changes in the past source distribution.

2 New data

Figure 1 presents the two new high-resolution atmospheric CH_4 records measured along the NGRIP (blue, 469 new measurements) and EDML (red, 190 new measurements) ice cores covering the time interval between 32 and 11 thousand years before present (kyr BP) on the unified EDML gas age scale derived by Lemieux-Dudon et al. (2010). This includes the Younger Dryas (YD), the Bølling/Allerød (BA), the LGM and the response to the DO events 2, 3, and 4. Earlier published EDML data (EPICA Community Members, 2006) are included in our calculations, where 83 remeasurements show a mean difference of 0.3 ppbv and a standard deviation of 13.9 ppbv. Few NGRIP data published earlier (Schilt et al., 2010b) are included as well. The mean time resolution is 43 years (yr) for NGRIP and 59 yr for EDML on the unified EDML gas age scale derived by Lemieux-Dudon et al. (2010). This is in the order of the width of the gas age distributions of the enclosed air from NGRIP and EDML and thus represents about the maximum resolution possible. Details about the measurement system are described in Sect. 2.3.

2.1 Synchronisation

Precise synchronisation between the ice cores from Greenland and Antarctica is a prerequisite to calculate the *IPD* of CH_4. The fast and strong variations in the greenhouse gas CH_4 can be used to synchronise the gas ages from different ice cores (Blunier et al., 2007). Ironically, the existence of the *IPD*, which we want to calculate based on a precise synchronisation, makes the latter one difficult, since for every tie point we assume a certain *IPD* value, which is a circular argument. Based on the assumption that fast CH_4 variations occur coincident in both hemispheres, our new high-resolution data improve the synchronisation of the NGRIP and EDML gas records. Particularly, a new tie point is defined at 20.9 kyr BP and the uncertainty of the tie points at the start and the end of DO event 2 is substantially reduced. We use 29 CH_4 tie points (Table 1, black triangles on top of Fig. 1) to improve the synchronisation of the NGRIP CH_4 record to the unified EDML gas age scale derived by Lemieux-Dudon et al. (2010). The start of the slow CH_4 increase at 18 kyr BP is also used as a tie point, assuming constant increase rates in both hemispheres. This assumption is not necessarily true, since the *IPD* represents an additional degree of freedom and induces a substantial synchronisation uncertainty in this case. We thus apply a synchronisation uncertainty of this tie point of 500 yr, which is much larger than that of rapid CH_4 changes ($\approx$ 50 yr).

2.2 Gravitational fractionation

In the context of the calculation of the *IPD* we have to discuss the gravitational fractionation in the firn column which decreases the CH_4 concentration at the close-off depth compared to the atmospheric value. The gravitational depletion in the considered time interval is relatively stable with mean values of 2.9 ± 0.6 ppbv for NGRIP and 2.4 ± 0.4 ppbv for EDML, where the close-off depth was calculated using the densification model by Herron and Langway (1980) with an estimated temperature and accumulation rate history from NGRIP (Johnsen et al., 2001; NGRIP Project Members, 2004) and EDML (Ruth et al., 2007; EPICA Community Members, 2006). The atmospheric

Title Page

Abstract | Introduction

Conclusions | References

Tables | Figures

◀ | ▶

◀ | ▶

Back | Close

Full Screen / Esc

Printer-friendly Version

Interactive Discussion

IPD would thus be about 0.5 ± 0.7 ppbv higher than the *IPD* measured in the ice cores. The effect on the relative interpolar difference (*rIPD*) is less than 0.1 %, which is small compared to the overall error. Thus, we do not correct the data for gravitational depletion.

2.3 Measurement system

We use a wet extraction technique according to Chappellaz et al. (1997) and Flückiger et al. (2004) to separate the enclosed air from the surrounding ice (sample size 40 g, corresponds to a depth interval of 3 and 5 cm, for EDML and NGRIP, respectively). In brief, a sample is put in a small glass container and after evacuation of the ambient air, the ice is melted at a temperature of 50 °C and refrozen from bottom to top at a temperature of −40 °C. The headspace volume is expanded into an evacuated and temperature-controlled (−60 °C) sampling loop and analysed by gas chromatography using a TCD ($N_2 + O_2 + Ar$) and FID (CH_4). Two standard gases (CH_4 concentration at 408 ppbv and 1050 ppbv) are used to calibrate the detectors at hourly intervals. Each calibration is checked by a control measurement with a third standard gas showing a mean concentration of 529.4 ± 3.1 ppbv over the entire measurement series. The reproducibility of measurements on natural ice samples was further determined by the analysis of series of 5 adjacent samples. 83 data points (corresponding to 18 depth intervals) show a precision of 6.2 ppbv, where 7 points have been rejected because of too high values caused by badly sealed glass containers (more than 3σ higher than the mean of the other reproducibility measurements from the same depth-interval).

3 Interpolar concentration difference of CH_4

The interpolar concentration difference of CH_4 is a valuable additional parameter which allows to constrain the geographical location of the responsible CH_4 sources. For the determination of the *IPD* of only a few ppbv we must exclude any systematic offsets

between the CH$_4$ records from both polar ice sheets. The sampling and measurement strategy of this study was designed for an optimum determination of the *IPD*. For the first time, all the new data points are analysed in the same laboratory, relative to the same standard gases and within the same year of measurement. On each measurement day we analysed both, samples from Greenland and Antarctica. Samples of different ages were measured in randomised order over the complete record to avoid systematic drifts in the *IPD*. Due to the quasi simultaneously analysed samples we are quite confident of the accuracy of the new *IPD* values. Note that there are still potential systematic error sources like in situ production in one of the records.

3.1 Definition and calculation of *IPD* and *rIPD*

We define the interpolar concentration difference of CH$_4$ in an absolute (*IPD*) and a relative manner (*rIPD*) similar to Brook et al. (2000):

$$IPD = c_n - c_s \tag{1}$$

$$rIPD = \frac{c_n - c_s}{\frac{1}{2}(c_n + c_s)} = \frac{IPD}{\frac{1}{2}(c_n + c_s)} \tag{2}$$

where c_n (index n: Northern Hemisphere) and c_s (index s: Southern Hemisphere) represent the concentrations measured along the NGRIP and EDML ice cores, respectively.

As described in Sect. 2.1 the synchronisation uncertainty is relatively small for most of the tie points. However, the CH$_4$ synchronisation provides no information about the timing between the tie points, where linear interpolation must be assumed. Therefore, we calculate c_n, c_s, and the *IPD* as means over specific time intervals instead of a continuous *IPD* record. In doing so, we essentially assume constant CH$_4$ levels within the intervals. The uncertainty in the *IPD* is dependent both on the measurement and the

synchronisation error. For the EDML measurement error, we assign the standard error of the mean to the mean value c_s of an interval. For the NGRIP record we use a Monte-Carlo approach to estimate the synchronisation error. For a total of 10^5 simulations, we randomly change the NGRIP start and end points of each interval. With the exception of the point at 24.4 kyr BP, these start and end points coincide with the tie points. For each simulation, the new NGRIP tie points are chosen randomly and uniformly distributed within the synchronisation uncertainty around the original tie points. Hereby, we assign a slightly different gas age to all NGRIP data points. For each simulation $i = 1 \ldots 10^5$ and time interval, the mean concentration $c_{n,i}$ and the standard error SE_i of the mean concentration are calculated. The final mean NGRIP concentration c_n and its measurement error is the mean of all simulations. The synchronisation error is calculated as the standard deviation of all simulations. Errors for the *IPD* and *rIPD* are calculated from c_n, c_s and the synchronisation error.

The criterion of constant CH_4 levels is not a reasonable assumption for the interval 17.8–14.8 kyr BP, where the CH_4 concentrations in both hemispheres show approximately a linear increase. We thus calculate the *IPD* as the mean difference between two linear fits through the data. In order to account for synchronisation uncertainties the NGRIP tie points are varied and the error of the *IPD* is obtained as the standard deviation of all 10^5 simulated *IPD* values.

Since the DO events 3 and 4 are too short to calculate a mean value over their duration, we estimate the *IPD* using the maximum atmospheric concentrations observed during the events (for more details see Sect. 3.4).

3.2 *IPD* in specified time intervals

A complete list of specified time intervals (I)–(XII), which correspond to the green shaded areas (plus DO events 3 and 4) in Fig. 1, and associated *IPD* and *rIPD* values are given in Table 2. We observe a positive *IPD* and hence a predominance of northern hemispheric sources compared to southern hemispheric sources throughout the record. Beside the very low *IPD* value during DO event 3, which has a large

uncertainty, the minimum *IPD* of 13.8 ± 2.5 ppbv (3.7 ± 0.7 %) is observed just after DO event 2 (interval VI), which is within the time interval of maximum ice sheet extent (Clark et al., 2009). The maximum *IPD* of 43.5 ± 6.5 ppbv (6.6 ± 1.0 %) is observed during the BA (interval II).

We refrain from calculating the *IPD* in the time interval 24.4–23.2 kyr BP because the EDML data are inconsistent with the Talos Dome Ice Core Project (TALDICE) data (Buiron et al., 2011; Stenni et al., 2011). This inconsistency is marked as the grey shaded interval in Fig. 2. Before DO event 2, TALDICE (yellow) and NGRIP (blue) show an increase in the CH_4 concentration from 26 kyr BP until the onset of DO event 2. This pattern is visible in EDML (red) prior to 24 kyr BP, however, just before DO event 2, the concentration level drops suddenly to 365.2 ppbv corresponding to the grey shaded area in Fig. 2. Remeasurements of the EDML samples in this 20 ppbv concentration dip confirm the low concentration level and exclude a problem in the measurement system. With the current time resolution of the TALDICE record, the EDML dip can not be entirely rejected. High-resolution measurements on other Antarctic ice cores will be crucial to resolve this issue. We note that TALDICE data suggest that the *IPD* would be similar as in the interval before.

3.3   Comparison with previous results

Figure 3 shows a compilation of new and existing (Brook et al., 2000; Chappellaz et al., 1997; Dällenbach et al., 2000) *rIPD* values. The new *rIPD* values between 21.9–17.8 kyr BP are in agreement with Brook et al. (2000) but are significantly larger than the estimate from Dällenbach et al. (2000). This difference results from a concentration offset between our new NGRIP data and the previously measured Greenland Ice Core Project (GRIP) data (Blunier et al., 1998; Dällenbach et al., 2000). Figure 2 shows that the GRIP data (light blue line) tend to be up to 30 ppbv lower than the NGRIP data (blue line) in certain time intervals. The GRIP data especially shows a larger bias towards lower concentrations. On the other hand, Antarctic records are consistent with the new EDML data. We remeasured 18 data points (round light blue symbols) along

the GRIP ice core and found a good agreement with our new NGRIP concentration level. A contamination of the GRIP ice due to the long storage time and an accompanying gas loss (Bereiter et al., 2009) is unlikely, since we eliminated about 5 mm of the outer surface when preparing the ice. The reliability among the new data emphasises the importance of measuring both hemispheric records in the same laboratory, with the same extraction technique, and using the same standard gases to correctly determine the *IPD*.

The *rIPD* values of the DO events 2 (7.1 ± 0.5 %) and 4 (6.2 ± 2.4 %) are well in the range of previous results from Brook et al. (2000) for DO event 8 (7.8 ± 2.0 %) and with the mean value over several DO events (7.5 ± 2.1 %) from Dällenbach et al. (2000). The *rIPD* value for DO event 3 (2.9 ± 2.3 %) is lower but has a large uncertainty.

For the BA period, we find a *rIPD* value twice as large as estimated by Brook et al. (2000) and Dällenbach et al. (2000). For the YD period, the new *rIPD* value is in agreement with Dällenbach et al. (2000) and 1.5 times larger than the value from Brook et al. (2000).

3.4   *IPD* during the DO events 3 and 4

In contrast to the other parts of the new CH_4 record, the DO events 3 and 4 are too short to calculate the *IPD* as a mean over a specific time interval. Thus, we estimate the interstadial *IPD* using an estimate of the maximum atmospheric concentrations observed during the events. However, because such fast and short atmospheric variations are attenuated due to molecular diffusion and gradual bubble close-off in the firn of an ice sheet, we first apply a forward smoothing firn model (Schwander et al., 1993; Spahni et al., 2003) to take into account the different enclosure characteristics of the EDML and the NGRIP sites. Temperature and accumulation rate, which both strongly influence the firn structure are assumed to be similar at both sites during stadial conditions. During the DO events 3 and 4 both, temperature ($-43.6 ± 4.8\,^\circ$C) and accumulation rate ($0.086 ± 0.023$ m of water equivalent yr^{-1}) jump up to higher values in the NGRIP ice core. The estimates are taken from the ss09sea age scale

(Johnsen et al., 2001) based on the δ^{18}O reconstructions (NGRIP Project Members, 2004) combined with the temperature-δ^{18}O relationship derived from δ^{15}N measurements (Huber et al., 2006). The higher temperature and accumulation rate during the interstadial periods leads to weaker attenuation at NGRIP compared to the EDML

5 site, where we assume a temperature of $-50.2 \pm 1.7\,°C$ and an accumulation rate of $0.036 \pm 0.006\,m$ of water equivalent yr^{-1} (EPICA Community Members, 2006; Ruth et al., 2007). Without application of the firn model, the *IPD* would be overestimated for these two short interstadial periods. Consequently, the interstadial *rIPD* recorded in the ice cores without enclosure correction represents an upper limit, which is 6.3 % for DO

10 event 3 and 9.3 % for DO event 4.

The application of the firn model helps to derive the interstadial *IPD* for DO event 3 and 4 more precisely. The model needs several input parameters. For the close-off density, the surface density and the tortuosity at NGRIP and EDML we use the values specified by Spahni et al. (2003) for GRIP and EPICA Dome C, respectively.

15 Since we use a forward smoothing model, we first need to estimate the atmospheric signal, which serves as input for the firn model. The atmospheric signal is then attenuated due to molecular diffusion and gradual bubble close-off in the firn (Schwander et al., 1993). The closed-off concentration, which we measure, is different compared to the original atmospheric concentration. Note that the estimation of the atmospheric

20 signal has no unique solution, since mathematically it is a deconvolution. We follow Spahni et al. (2003) and simply linearly scale the NGRIP signal to construct the estimate of both, the northern and southern atmospheric signal. The constructed northern atmospheric signal is the input for the firn model at the NGRIP site, where we apply three different attenuation scenarios (mean [min,max]; Fig. 4). The smallest root mean

25 square difference between the output of the firn model and the measured NGRIP data is achieved when the linear scaling factor is 1.13 [1.06,1.19] for DO event 3 and 1.08 [1.05,1.13] for DO event 4. The southern atmospheric signal, which is obtained by linear scaling of the NGRIP signal as well, is the input for the firn model at the EDML site, where we apply again three different attenuation scenarios (mean [min,max]). The

output of the firn model is shifted to lower concentration until the smallest root mean square difference to the measured EDML data is achieved. This is the case when the linear scaling factor is 1.48 [1.35,1.62] for DO event 3 and 1.11 [1.02,1.21] for DO event 4. The resulting *IPD* (13.4 ± 10.7 ppbv for DO event 3 and 31.4 ± 12.1 ppbv for DO event 4) is calculated as the difference between the maximum concentrations of the splines (cutoff period 100 yr) through the atmospheric input signals, where the maximum attenuation at NGRIP is combined with the minimum attenuation at EDML and vice versa. The resulting *rIPD* is (2.9 ± 2.3 %) for DO event 3 and (6.2 ± 2.4 %) for DO event 4.

4   Source distribution of CH$_4$

The new NGRIP and EDML records provide the concentrations of CH$_4$ in the northern (c_n) and southern (c_s) hemispheres. This enables us to formulate a two-box model to estimate the CH$_4$ source strength in the northern (s_n) and southern (s_s) hemispheres. In this two-box model, the northern box (0° N–90° N, index: n) and the southern box (0° S–90° S, index: s) account for 50 % of the total atmospheric volume each. The mass balance (Tans, 1997) is given by:

$$\frac{dM}{dt} = S - \mathbf{\Omega} \cdot M \tag{3}$$

$$M = \frac{m_0}{c_0} \cdot \begin{pmatrix} c_n \\ c_s \end{pmatrix} \; , \quad S = \begin{pmatrix} s_n \\ s_s \end{pmatrix} \tag{4}$$

$$\mathbf{\Omega} = \begin{pmatrix} \frac{1}{\tau} + \frac{1}{t_{ex}} & -\frac{1}{t_{ex}} \\ -\frac{1}{t_{ex}} & \frac{1}{\tau} + \frac{1}{t_{ex}} \end{pmatrix} \tag{5}$$

where τ is the atmospheric lifetime of CH$_4$, and t_{ex} the interhemispheric mixing time. We initialise the model with today's source distribution from Fung et al. (1991) and find

$\tau = 10.1\,\text{yr}$ and $t_{ex} = 2\,\text{yr}$. The dependence of s_n and s_s on these parameters is described in Sect. 4.1. The ratio $m_0/c_0 = 1.45\,\text{Tg/ppbv}$ (Steele et al., 1992) converts the concentration (ppbv) into mass (Tg box^{-1}). The model is run for steady state conditions, which simplifies Eq. (3) and provides the sources:

$$s_n(c_n, IPD, \tau, t_{ex}) = \frac{m_0}{c_0} \cdot \left(\frac{1}{\tau} \cdot c_n + \frac{1}{t_{ex}} \cdot IPD \right) \tag{6}$$

$$s_s(c_s, IPD, \tau, t_{ex}) = \frac{m_0}{c_0} \cdot \left(\frac{1}{\tau} \cdot c_s - \frac{1}{t_{ex}} \cdot IPD \right) \tag{7}$$

The calculated source strengths corresponding to the mean concentrations of the specified time intervals (Fig. 1) are summarised in Table 2. The errors for s_n and s_s in this top-down simulation are calculated from the errors of c_n and c_s.

Vice versa in a bottom-up simulation, from a given source distribution the two-box model provides the concentrations c_n, c_s and the IPD and $rIPD$:

$$IPD(s_n, s_s, \tau, t_{ex}) = \frac{c_0}{m_0} \cdot (s_n - s_s) \cdot \frac{\tau}{1 + 2\frac{\tau}{t_{ex}}} \tag{8}$$

$$rIPD(s_n, s_s, \tau, t_{ex}) = 2 \cdot \frac{s_n - s_s}{s_n + s_s} \cdot \frac{1}{1 + 2\frac{\tau}{t_{ex}}} \tag{9}$$

Hence in this two-box model both the IPD and the $rIPD$ are proportional to the difference $s_n - s_s$, but only the $rIPD$ is independent on global source scaling. This implies that if s_n and s_s are scaled by the same factor, the $rIPD$ stays constant.

For short exchange times t_{ex} the influence of τ on the IPD is of minor importance. Consequently, the $rIPD$ (see Eq. 2) decreases with increasing atmospheric lifetime τ, since a higher atmospheric lifetime induces a higher atmospheric concentration.

4.1 Sensitivity of CH_4 sources to τ and t_{ex}

Figure 5 shows the sensitivity of the sources s_n and s_s calculated in Eq. (6) and Eq. (7) on the parameters τ and t_{ex} for three different time intervals (BA, YD, LGM). Relatively small changes in the two parameters have substantial impact on the estimated sources. For both parameters, the sensitivity is stronger for higher *IPD*. Note that other studies using a two-box model (Sowers, 2010) lower the concentration measured in Greenland c_n by a fixed portion of the *IPD* to obtain the mean concentration of the northern box. This takes into account the decreasing concentration within the northern box observed today. Due to the lack of the anthropogenic sources, this latitudinal concentration gradient might have been smaller in the past, however, it might still have been present since it is mainly an effect of the sink, which is significantly lower at high latitudes. We did not lower the ice core derived c_n in our model study, but took this effect into account in our model tuning by allowing for a relatively large t_{ex} of 2 yr. This essentially implies that this exchange time is representing the time needed for CH_4 to sustain the measured interpolar and not a mean interhemispheric concentration difference.

5 Discussion

Figure 6 summarises the results of this study. Figure 6a shows the two new NGRIP and EDML CH_4 concentration records again for reference, and Fig. 6b displays the resulting source strengths. To put the variations in the concentration, *IPD* and *rIPD* on a common scale, we define interval (V) (20.4–17.8 kyr BP) as the reference interval (index ref) and calculate the ratios $c_s/c_{s,ref}$, IPD/IPD_{ref} and $rIPD/rIPD_{ref}$ (Fig. 6d). The variations in the *rIPD* and CH_4 source strength are compared with the variations in the speleothem monsoon records from Hulu cave (China) at 32° N (Wang et al., 2001) and Pacupahuain Cave (Peru) at 11° S (Kanner et al., 2012), the isotopic composition ($\delta^{13}CH_4$) of CH_4 (Fischer et al., 2008), and the benthic $\delta^{18}O$ record from Lisiecki and Raymo (2005), which are shown in Fig. 6c. The monsoon records provide important information on the

availability of water in the major tropical CH_4 source regions. The isotopic composition of CH_4 together with the *IPD* is influenced by the strength of the boreal emissions (Fischer et al., 2008), however, also changes in the isotopic signature of individual methane sources over time may lead to such changes (Schaefer and Whiticar, 2008). The benthic $\delta^{18}O$ record, which is a proxy for global ice volume, provides information about the ice coverage of the boreal emission regions.

5.1 Variations in the *rIPD* and CH_4 source strength

In general, we observe a relatively stable *rIPD* value throughout the record (Fig. 3). In particular, there is less variability in the *rIPD* than in earlier studies, since we showed that the previously measured *rIPD* value during the LGM (Dällenbach et al., 2000) was too low (Sect. 3.3). The stability of the *rIPD* is also expressed in Fig. 6d, which shows that the ratio $rIPD/rIPD_{ref}$ (pink curve) is not different from 1 for the majority of the time intervals. The ratio IPD/IPD_{ref} (green curve) on the other hand shows a relatively large correlation ($R^2 = 0.8$) with the normalised CH_4 concentration $c_s/c_{s,ref}$ (red curve). This points to a relatively stable source distribution despite changing total emission strengths, i.e. if the concentration changes, the sources s_n and s_s change by a similar factor.

Despite the overall stability, we subdivide the *rIPD* record into two periods. In the first period (28–21 kyr BP) the *rIPD* tends to be lower with exception of DO event 2, which is discussed in Sect. 5.1.4 together with other DO events. In the second period (21–11 kyr BP) including Termination 1 (T1), the *rIPD* tends to be higher.

5.1.1 Lower *rIPD* state in the LGM

With the exception of DO event 2, the *rIPD* is slightly reduced between 28–21 kyr BP compared to the reference value (Fig. 6d). Especially in North America, the boreal source is likely to be suppressed by the wide extent of the ice sheets and permafrost regions and hence is likely to contribute to the reduction of the *rIPD* (Dällenbach et al.,

2000; Fischer et al., 2008). Further, a bottom-up modelling study supports a southward shift of the boreal and tropical sources in the LGM, which was caused by a southward shift of the westerlies because of the large ice sheet extent and by a southward displacement of the ITCZ, respectively (Weber et al., 2010). A southward displacement of the ITCZ could influence the *rIPD* in two ways. First, it would shift the optimal conditions for CH_4 emissions to more southerly latitudes. The effect on the *rIPD* might be amplified by the coincident latitudinal dislocation of the monsoon systems. Second, a southward shift in the ITCZ would increase the volume of the northern box on the cost of the southern box. A 1° southward shift would change the volumes and thus the concentrations in the northern and southern box by about 2 % in opposite directions. Further, the same change in CH_4 emitted in the northern box would result in a lower concentration change in the northern box due to this volume increase.

During the Holocene, speleothem records from the Northern Hemisphere (Southern Hemisphere) show a long-term decrease (increase) in precipitation in line with Northern Hemisphere (Southern Hemisphere) summer insolation (Burns, 2011). This points to a long-term southward shift of the mean position of the ITCZ during the Holocene. Singarayer et al. (2011) use this southward shift of the ITCZ to explain the increase in the CH_4 concentration during the Holocene which started at 5 kyr BP. While the northern source strength remains at a constant level they state that the additional emissions stem from the Southern Hemisphere due to wetter conditions. This scenario of southward shift of the ITCZ is supported by the reduction of the *rIPD* from the Mid Holocene to the Preindustrial Holocene, where the temporarily higher *rIPD* during the Late Holocene was attributed to boreal wetland expansion (Burns, 2011; Chappellaz et al., 1997).

Similarly as during the Preindustrial Holocene, the Southern Hemisphere summer insolation reaches a maximum at 20 kyr BP. As in the Holocene, the enhanced precipitation connected to this maximum in the southern low latitudes could boost the emissions from the Southern Hemisphere. Indeed the summer monsoon strength at Pacupahuain cave (South America) is relatively high (compared to the full glacial record)

while the summer monsoon strength at Hulu cave (China) is very weak during this period (Fig. 6c). In line the fraction of the southern CH_4 emission on the total emissions is relatively high compared to the other parts of the record in our two-box model (Fig. 6b).

5.1.2   *rIPD* increase around 21 kyr BP

Around 21 kyr BP we observe a strong increase in the *rIPD*, just after the pronounced minimum in the *rIPD* between 21.9–21.2 kyr BP. From a strictly CH_4 point of view this minimum refers to the smallest boreal wetland emissions and hence marks the glacial maximum in the CH_4 cycle. The subsequent increase in the *rIPD* happens several thousand years before the transition into the Holocene and in the absence of rapid climatic changes like a DO event, although we recognize a small peak in the CH_4 concentration at 21 kyr BP (Fig. 1). The increase in the mean CH_4 concentration from the time interval 21.9–21.2 kyr BP to the time interval 20.4–17.8 kyr BP is only 15 ppbv. The consequent increase in s_{tot} of $4\,\mathrm{Tgyr^{-1}}$ arises from an increase in s_n of $10\,\mathrm{Tgyr^{-1}}$ and a simultaneous decrease in s_s of $6\,\mathrm{Tgyr^{-1}}$ in our two-box model. The coincident decreasing and increasing trend in the southern and northern summer monsoon strength derived from speleothems (Fig. 6c) starting at 21 kyr BP, respectively, could contribute to the increase in the *rIPD*. Note, however, that we have to be careful in comparing speleothem records with gas records from ice cores due to synchronisation uncertainties.

5.1.3   Higher *rIPD* state during Termination 1

The new data suggest a fairly stable mean *rIPD* level of $6.5 \pm 0.8\,\%$ (20.4–11.7 kyr BP, intervals (I)–(V)) during T1, which is well expressed in the ratio $rIPD/rIPD_{ref}$ close to one (Fig. 6d). With the exception of the higher value during the late Holocene, previous Holocene reconstructions show a similar *rIPD* as well (Chappellaz et al., 1997). It is also close to the present day anthropogenicly modified *rIPD* (7 %) with global emissions twice as large. Taken at face value and assuming a constant atmospheric lifetime (Levine et al., 2011) and interhemispheric mixing time, this could imply that the source

distributions of the Holocene, BA and YD period were not so different from the source distribution at the end of the last glacial (20.4–17.8 kyr BP). Note that the YD period still shows the lowest *rIPD* during T1 in line with Northern Hemisphere cold conditions. On the other hand, the BA shows a relatively high *rIPD* despite a still more extended

5 northern continental ice coverage in the BA compared to the Holocene.

The interval 17.8–14.7 kyr BP (IV), which contains Heinrich event 1 (H1) and shows a slow 100 ppbv increase in the CH_4 concentration, has also a relatively high *rIPD* value although with a large uncertainty due to the synchronisation uncertainty (Sects. 2.1 and 3.1). To agree with both, the higher concentration and the higher *rIPD* value compared

10 to the glacial reference interval (20.4–17.8 kyr BP), an increase in s_n is needed.

There are three arguments in support of an increase in s_n due to higher boreal emissions. First, the catastrophic drought in Afro-Asian monsoon regions (Stager et al., 2011; Wang et al., 2001) related to H1 tends to weaken the low-latitude northern source. Second, 75 % of the glacial to Holocene decrease in the isotopic signature

15 $\delta^{13}CH_4$ (Fig. 6c) occurs within this interval (Fischer et al., 2008) which points to an increase in the boreal CH_4 source. Note, however, that the interpretation of $\delta^{13}CH_4$ is not yet unambiguous and that, for instance, a large shift in the ratio of C3 to C4 plants could also explain the isotopic changes over T1 (Sowers, 2010; Schaefer and Whiticar, 2008). Third, the increase in the benthic $\delta^{18}O$ (Lisiecki and Raymo, 2005) represents

20 the start of the deglaciation and the boreal regions start to loose their ice coverage along with a northward migration of permafrost. A large portion (Fig. 6c) of the LGM-to-Holocene benthic $\delta^{18}O$ increase is already completed by the beginning of the BA period.

5.1.4 *rIPD* variations during DO events

25 The lower *rIPD* state between 28–21 kyr BP is interrupted by DO event 2 (7.1 ± 0.5 %). The increase in the concentration is caused by an increase in s_n of 12 Tg yr^{-1} and a slight decrease in s_s by 4 Tg yr^{-1} in our model. During DO events, the active AMOC

transports heat into the Northern Hemisphere, which should enhance the northern CH_4 emissions. According to Dällenbach et al. (2000), the higher *rIPD* values during DO events are caused by a strong increase in the boreal source strength. In this context, the equally high *rIPD* value for DO event 2 compared to other DO events (Sect. 3.3) is surprising, since DO event 2 occurs in a time of very large ice sheet extent and, thus, an equally strong impact of boreal wetland sources appears not to be straightforward. Thus, the question arises if the boreal emissions during DO events have been overestimated. Several studies (Otto-Bliesner and Brady, 2010; Broccoli et al., 2006; Schmidt and Spero, 2011) suggest also latitudinal swings in the ITCZ and the monsoon systems on millennial time scales. During DO events, the ITCZ is located in a more northward position coincident with increased northern summer monsoon strength compared to the cold stadial intervals. The strong anti-correlation on millennial time scales of the monsoon records from Hulu cave (China) and Pacupahuain cave (South America) corroborates this statement (Kanner et al., 2012). The anti-correlation during DO event 2 is less clear than for other DO events like DO event 4 (Fig. 6c). While there are two contemporary decreases in the southern summer monsoon strength (Fig. 6c), which could be attributed to DO event 2, a clear peak in the northern summer monsoon strength is missing, although we see a recovery from Heinrich event 2 (H2) in the $\delta^{18}O$ speleothem record. No reduction of the southern summer monsoon strength is observed during DO event 3 (Kanner et al., 2012). This is in line with the lower *rIPD* value during DO event 3. We thus hypothesise that the source redistribution within lower latitudes connected to shifts in the ITCZ also contributes to the variations in the *rIPD*.

Despite the good correlation of the CH_4 concentration and the speleothem records on millennial time scales, it remains unclear why we do not see an impact in the CH_4 concentration or in the *rIPD* during Heinrich events, where the southward displacement of the ITCZ is exceptionally strong.

5.1.5 Long-term *rIPD* trend

In this section we discuss a potential long-term influence of the ratio of northern to southern summer insolation (I_{ns}/I_{ss}) on the latitudinal distribution of the CH_4 sources. If such an influence exists, it should be mirrored in the *rIPD* data (see Fig. 7). In periods of low I_{ns}/I_{ss}, we would expect higher emissions from the Southern Hemisphere due to longer emission seasons in the south. As already discussed in Sect. 5.1.1, the lower *rIPD* state between 28–21 kyr BP is approximately at the time of a minimum in I_{ns}/I_{ss}. Further, neglecting the higher *rIPD* during the Late Holocene, which has been attributed to boreal wetland expansion (Chappellaz et al., 1997), the maximum in the *rIPD* data occurs around 14 kyr approximately at the time of a maximum in I_{ns}/I_{ss}. The long-term decrease in the *rIPD* during the Holocene towards the next minimum in I_{ns}/I_{ss} supports a long-term trend of the *rIPD* in parallel to I_{ns}/I_{ss}. Looking again at the interval 30–20 kyr BP (Fig. 7) we could identify a similar decreasing long-term trend as during the Holocene. Nonetheless, if such a long-term trend exists in our data it is very weak and our new data set goes not far enough back in time to enable a comparison with the time scale of the precessional cycle. Further, the DO event 2 and the Late Holocene are clearly outstanding, which points to superimposed processes on shorter time scales.

A model simulation much longer back in time is given in a bottom-up modeling study by Singarayer et al. (2011), who estimated the CH_4 emissions over the last 120 kyr BP for different source regions. Their model accounts for orbital forcing, greenhouse gas concentrations, ice sheet extent and sea level, but it neglects millennial scale variability. To asses a long-term trend in the *rIPD* from their results, we use the sum of all northern and southern hemispheric emissions in the Singarayer et al. (2011) study as an input for our two-box model for the northern and the southern box, respectively. The estimated *rIPD* (orange line in Fig. 7) shows a clear variation along with the precessional cycle. Compared to our data, the amplitude of the modeled precessional *rIPD* variation seems to be overestimated or at least biased during the glacial. Nonetheless, it does not exclude that there could be a long-term component in the *rIPD* signal.

Apart from DO event 2, the statement of a long-term component of the *rIPD* in parallel to summer insolation could still be valid for DO events. Brook et al. (1996) and Flückiger et al. (2004) suggested that I_{ns}/I_{ss} determines the CH_4 amplitude of DO events, yielding higher amplitudes for DO events 5–8 and 15–17 compared to DO events 9–12. High-resolution records produced in the way presented here from both poles, and over DO events 5–17, would be most interesting to address this question. The importance of the *rIPD* as a constraint for models is a strong motivation for future high-resolution measurements over the whole last glacial cycle.

6 Conclusions

The sampling and measurement strategy carried out for this study was designed for an optimum determination of the interpolar difference of CH_4. The quasi simultaneously analysed samples from Greenland and Antarctica increase the confidence in the accuracy of our values. We suggest that this procedure is essential for future *rIPD* studies. Further, the high resolution of our records improves the synchronisation of the gas ages between the NGRIP and EDML ice cores and determines the *IPD* with unprecedented precision and temporal resolution.

We show that the previous *rIPD* estimate ($-0.8 \pm 1.0\%$) during the LGM (21.9–17.8 kyr BP) from Dällenbach et al. (2000) was significantly too low. The revised estimate is between $3.7 \pm 0.7\%$ and $6.1 \pm 0.5\%$. Consequently, there is less variability in the *rIPD* and CH_4 source distribution than previously reported and boreal wetland sources in the Northern Hemisphere were never completely shut off during the glacial. The strongest variations in the *rIPD* (28–18 kyr BP) are observed during a time interval, where only smaller DO changes in the CH_4 concentration occurred. The lowest *rIPD* ($3.7 \pm 0.7\%$) is observed between 21.9–21.2 kyr BP just after DO event 2. This is during a time when the ice sheet extent was at its maximum and the northern-to-southern summer insolation ratio at its minimum. A shift back to northern sources

happens around 21 kyr BP coincident with decreasing southern and increasing northern summer monsoon strength.

The *rIPD* during Termination 1 is fairly stable (6.5 ± 0.8 %), although somewhat lower during the YD. It is also close to the present day anthropogenicly modified *rIPD* (7 %) with global emissions twice as large. Assuming a constant atmospheric lifetime of CH_4 (Levine et al., 2011), the stability of the *rIPD* could imply that the interhemispheric source distribution of the Holocene was not so different from the source distribution of the last glacial, although with increasing source strengths both south and north of the equator.

The *rIPD* values for DO event 2 (7.1 ± 0.5 %) and 4 (6.2 ± 2.4 %) are well in the range of previous results for DO event 8 (7.8 ± 2.0 %) (Brook et al., 2000) and with the mean value over several DO events (7.5 ± 2.1 %) (Dällenbach et al., 2000). The *rIPD* value for DO event 3 (2.9 ± 2.3 %) is lower but has a large uncertainty connected to the short duration of this event.

We hypothesise that the anti-correlation observed in the monsoon records from the Northern and Southern Hemispheres induces a source redistribution within lower latitudes, which could explain parts of the variations in the *rIPD*.

Appendix A

Supplementary data

NGRIP and EDML CH_4 records can be downloaded from the website of the World Data Center for Paleoclimatology at www.ncdc.noaa.gov/paleo.

Supplementary material related to this article is available online at:
http://www.biogeosciences-discuss.net/9/5471/2012/
bgd-9-5471-2012-supplement.zip.

References

Bereiter, B., Schwander, J., Lüthi, D., and Stocker, T. F.: Change in CO_2 concentration and O_2/N_2 ratio in ice cores due to molecular diffusion, Geophys. Res. Lett., 36, L05703. doi:10.1029/2008GL036737, 2009. 5480

Bloom, A. A., Palmer, P. I., Fraser, A., Reay, D. S., and Frankenberg, C.: Large-scale controls of methanogenesis inferred from methane and gravity spaceborne data, Science, 327, 322–325, 2010. 5473

Blunier, T., Chappellaz, J., Schwander, J., Dällenbach, A., Stauffer, B., Stocker, T. F., Raynaud, D., Jouzel, J., Clausen, H. B., Hammer, C. U., and Johnsen, S. J.: Asynchrony of Antarctic and Greenland climate change during the last glacial period, Nature, 394, 739–743, 1998. 5479, 5502

Blunier, T., Spahni, R., Barnola, J.-M., Chappellaz, J., Loulergue, L., and Schwander, J.: Synchronization of ice core records via atmospheric gases, Clim. Past, 3, 325–330, doi:10.5194/cp-3-325-2007, 2007. 5475

Broccoli, A. J., Dahl, K. A., and Stouffer, R. J.: Response of the ITCZ to Northern Hemisphere cooling, Geophys. Res. Lett., 33, L01702, doi:10.1029/2005GL024546, 2006. 5489

Title Page

Abstract | Introduction

Conclusions | References

Tables | Figures

◄ | ►

◄ | ►

Back | Close

Full Screen / Esc

Printer-friendly Version

Interactive Discussion

Brook, E. J., Harder, S., Severinghaus, J., Steig, E. J., and Sucher, C. M.: On the origin and timing of rapid changes in atmospheric methane during the last glacial period, Global Biogeochem. Cy., 14, 559–572, 2000. 5474, 5477, 5479, 5480, 5492, 5503, 5508

Brook, E. J., Sowers, T., and Orchardo, J.: Rapid variations in atmospheric methane concentration during the past 110 000 years, Science, 273, 1087–1091, 1996. 5491

Buiron, D., Chappellaz, J., Stenni, B., Frezzotti, M., Baumgartner, M., Capron, E., Landais, A., Lemieux-Dudon, B., Masson-Delmotte, V., Montagnat, M., Parrenin, F., and Schilt, A.: TALDICE-1 age scale of the Talos Dome deep ice core, East Antarctica, Clim. Past, 7, 1–16, doi:10.5194/cp-7-1-2011, 2011. 5479, 5502

Burns, S. J.: Speleothem records of changes in tropical hydrology over the Holocene and possible implications for atmospheric methane, Holocene, 21, 735–741, 2011. 5486

Chappellaz, J., Blunier, T., Kints, S., Dällenbach, A., Barnola, J. M., Schwander, J., Raynaud, D., and Stauffer, B.: Changes in the atmospheric CH_4 gradient between Greenland and Antarctica during the Holocene, J. Geophys. Res.-Atmos., 102, 15987–15997, 1997. 5474, 5476, 5479, 5486, 5487, 5490, 5503, 5507, 5508

Clark, P. U., Dyke, A. S., Shakun, J. D., Carlson, A. E., Clark, J., Wohlfarth, B., Mitrovica, J. X., Hostetler, S. W., and McCabe, A. M.: The Last Glacial Maximum, Science, 325, 710–714, 2009. 5479

Dällenbach, A., Blunier, T., Flückiger, J., Stauffer, B., Chappellaz, J., and Raynaud, D.: Changes in the atmospheric CH_4 gradient between Greenland and Antarctica during the Last Glacial and the transition to the Holocene, Geophys. Res. Lett., 27, 1005–1008, 2000. 5474, 5479, 5480, 5485, 5489, 5491, 5492, 5502, 5503

Denman, K., Brasseur, G., Chidthaisong, A., Ciais, P., Cox, P., Dickinson, R., Hauglustaine, D., Heinze, C., Holland, E., Jacob, D., Lohmann, U., Ramachandran, D., da Silva Dias, P., Wofsy, S., and Zhang, X.: Couplings between changes in the climate system and biogeochemistry, in: Climate Change 2007: The Physical Science Basis, Contribution of Working Group I to the Fourth Assessment Report of the Intergovernmental Panel on Climate Change, 2007. 5473

Dlugokencky, E. J., Lang, P. M., and Masarie, K. A.: Atmospheric Methane Dry Air Mole Fractions from the NOAA ESRL Carbon Cycle Cooperative Global Air Sampling Network, 1983–2010, Path: ftp://ftp.cmdl.noaa.gov/ccg/ch4/flask/event/, Version: 2011-08-11, 2011. 5473

Enting, I.: On the use of smoothing splines to filter CO_2 data, J. Geophys. Res.-Atmos., 92, 10977–10984, 1987. 5501

Interpolar difference of atmospheric methane

M. Baumgartner et al.

Title Page

Abstract	Introduction
Conclusions	References
Tables	Figures

Back | Close

Full Screen / Esc

Printer-friendly Version

Interactive Discussion

Barbante, C., Barnola, J.-M., Becagli, S., Beer, J., Bigler, M., Boutron, C., Blunier, T., Castellano, E., Cattani, O., Chappellaz, J., and Dahl-Jensen, D., Debret, M., Delmonte, B., Dick, D., Falourd, S., Faria, S., Federer, U., Fischer, H., Freitag, J., Frenzel, A., Fritzsche, D., and Fundel, F., Gabrielli, P., Gaspari, V., Gersonde, R., Graf, W., Grigoriev, D., Hamann, I., Hansson, M., Hoffmann, G., Hutterli, M. A., Huybrechts, P., Isaksson, E., Johnsen, S., Jouzel, J., Kaczmarska, M., Karlin, T., Kaufmann, P., Kipfstuhl, S., Kohno, M., Lambert, F., Lambrecht, Anja, Lambrecht, Astrid, Landais, A., Lawer, G., Leuenberger, M., Littot, G., Loulergue, L., Lüthi, D., Maggi, V., Marino, F., Masson-Delmotte, V., Meyer, H., Miller, H., Mulvaney, R., Narcisi, B., Oerlemans, J., Oerter, H., Parrenin, F., Petit, J.-R., Raisbeck, G., Raynaud, D., Roethlisberger, R., Ruth, U., Rybak, O., Severi, M., Schmitt, J., Schwander, J., Siegenthaler, U., Siggaard-Andersen, M.-L., Spahni, R., Steffensen, J. P., Stenni, B., Stocker, T. F., Tison, J.-L., Traversi, R., Udisti, R., Valero-Delgado, F., van den Broeke, M. R., van de Wal, R. S. W., Wagenbach, D., Wegner, A., Weiler, K., Wilhelms, F., Winther, J.-G., Wolff, E., and EPICA Community Members: One-to-one coupling of glacial climate variability in Greenland and Antarctica, Nature, 444, 195–198, 2006. 5474, 5475, 5481, 5501, 5502, 5507

Fischer, H., Behrens, M., Bock, M., Richter, U., Schmitt, J., Loulergue, L., Chappellaz, J., Spahni, R., Blunier, T., Leuenberger, M., and Stocker, T. F.: Changing boreal methane sources and constant biomass burning during the last termination, Nature, 452, 864–867, 2008. 5484, 5485, 5486, 5488, 5507

Flückiger, J., Blunier, T., Stauffer, B., Chappellaz, J., Spahni, R., Kawamura, K., Schwander, J., Stocker, T. F., and Dahl-Jensen, D.: N_2O and CH_4 variations during the last glacial epoch: insight into global processes, Global Biogeochem. Cy., 18, GB1020, doi:1029/2003GB002122, 2004. 5476, 5491

Fung, I., John, J., Lerner, J., Matthews, E., Prather, M., Steele, L., and Fraser, P.: 3-Dimensional model synthesis of the global methane cycle, J. Geophys. Res.-Atmos., 96, 13033–13065, 1991. 5482, 5505

Hein, R., Crutzen, P. J., and Heimann, M.: An inverse modeling approach to investigate the global atmospheric methane cycle, Global Biogeochem. Cy., 11, 43–76, 1997. 5473

Hemming, S. R.: Heinrich events: massive late pleistocene detritus layers of the North Atlantic and their global climate imprint, Rev. Geophys., 42, RG1005, doi:10.1029/2003RG000128, 2004. 5501

Herron, M. M. and Langway, C. C.: Firn densification – an empirical-model, J. Glaciol., 25, 373–385, 1980. 5475

Huber, C., Leuenberger, M., Spahni, R., Flückiger, J., Schwander, J., Stocker, T. F., Johnsen, S., Landais, A., and Jouzel, J.: Isotope calibrated Greenland temperature record over Marine Isotope Stage 3 and its relation to CH_4, Earth Planet. Sc. Lett., 243, 504–519, 2006. 5481

Johnsen, S. J., Dahl-Jensen, D., Gundestrup, N., Steffensen, J. P., Clausen, H., Miller, H., Masson-Delmotte, V., Sveinbjornsdottir, A., and White, J.: Oxygen isotope and palaeotemperature records from six Greenland ice-core stations: Camp Century, Dye-3, GRIP, GISP2, Renland and NorthGRIP, J. Quaternary Sci., 16, 299–307, 2001. 5475, 5481

Kanner, L. C., Burns, S. J., Cheng, H., and Edwards, R. L.: High-latitude forcing of the South American summer monsoon during the Last Glacial, Science, 335, 570–573, 2012. 5484, 5489, 5507

Kaplan, J. O., Folberth, G., and Hauglustaine, D. A.: Role of methane and biogenic volatile organic compound sources in late glacial and Holocene fluctuations of atmospheric methane concentrations, Global Biogeochem. Cy., 20, GB2016, doi:10.1029/2005GB002590., 2006. 5473

Lemieux-Dudon, B., Eric, B., Jean-Robert, P., Claire, W., Anders, S., Catherine, R., Jean-Marc, B., Maria, N. B., and Frederic, P.: Consistent dating for Antarctic and Greenland ice cores, Quaternary Sci. Rev., 29, 2821–2822, 2010. 5474, 5475, 5499, 5501, 5502, 5503, 5507

Levine, J. G., Wolff, E. W., Jones, A. E., Sime, L. C., Valdes, P. J., Archibald, A. T., Carver, G. D., Warwick, N. J., and Pyle, J. A.: Reconciling the changes in atmospheric methane sources and sinks between the Last Glacial Maximum and the pre-industrial era, Geophys. Res. Lett., 38, L23804, doi:10.1029/2011GL049545, 2011. 5473, 5487, 5492

Lisiecki, L. and Raymo, M.: A Pliocene-Pleistocene stack of 57 globally distributed benthic delta O-18 records, Paleoceanography, 20, PA2007, doi:10.1029/2005PA001164, 2005. 5484, 5488, 5507

Andersen, K. K., Azuma, N., Barnola, J. M., Bigler, M., Biscaye, P., Caillon, N., Chappellaz, J., Clausen, H. B., DahlJensen, D., Fischer, H., Fluckiger, J., Fritzsche, D., Fujii, Y., Goto-Azuma, K., Gronvold, K., Gundestrup, N. S., Hansson, M., Huber, C., Hvidberg, C. S., Johnsen, S. J., Jonsell, U., Jouzel, J., Kipfstuhl, S., Landais, A., Leuenberger, M., Lorrain, R., Masson-Delmotte, V., Miller, H., Motoyama, H., Narita, H., Popp, T., Rasmussen, S. O., Raynaud, D., Rothlisberger, R., Ruth, U., Samyn, D., Schwander, J., and Shoji, H., and Siggard-Andersen, M. L., and Steffensen, J. P., and Stocker, T., and Sveinbjornsdottir, A. E., and Svensson, A., and Takata, M., and Tison, J. L., and Thorsteinsson, T., and Watanabe, O., and Wilhelms, F.,

Title Page

Abstract | Introduction

Conclusions | References

Tables | Figures

◄ | ►►|

◄ | ►

Back | Close

Full Screen / Esc

Printer-friendly Version

Interactive Discussion

and White, J. W. C., and N Greenland Ice Core Project: High-resolution record of Northern Hemisphere climate extending into the last interglacial period, Nature, 431, 147–151, 2004. 5475, 5481

Otto-Bliesner, B. L. and Brady, E. C.: The sensitivity of the climate response to the magnitude and location of freshwater forcing: Last Glacial Maximum experiments, Quaternary Sci. Rev., 29, 56–73, 2010. 5489

Quinn, T., Tremaine, S., and Duncan, M.: A 3 million year integration of the Earths orbit, Astron. J., 101, 2287–2305, 1991. 5507, 5508

Ruth, U., Barnola, J.-M., Beer, J., Bigler, M., Blunier, T., Castellano, E., Fischer, H., Fundel, F., Huybrechts, P., Kaufmann, P., Kipfstuhl, S., Lambrecht, A., Morganti, A., Oerter, H., Parrenin, F., Rybak, O., Severi, M., Udisti, R., Wilhelms, F., and Wolff, E.: "EDML1": a chronology for the EPICA deep ice core from Dronning Maud Land, Antarctica, over the last 150 000 years, Clim. Past, 3, 475–484, doi:10.5194/cp-3-475-2007, 2007. 5475, 5481

Schaefer, H. and Whiticar, M. J.: Potential glacial-interglacial changes in stable carbon isotope ratios of methane sources and sink fractionation, Global Biogeochem. Cy., 22, GB1001, doi:10.1029/2006GB002889, 2008. 5485, 5488

Schilt, A., Baumgartner, M., Blunier, T., Schwander, J., Spahni, R., Fischer, H., and Stocker, T. F.: Glacial-interglacial and millennial-scale variations in the atmospheric nitrous oxide concentration during the last 800 000 years, Quaternary Sci. Rev., 29, 182–192, 2010a. 5501

Schilt, A., Baumgartner, M., Schwander, J., Buiron, D., Capron, E., Chappellaz, J., Loulergue, L., Schüpbach, S., Spahni, R., Fischer, H., and Stocker, T. F.: Atmospheric nitrous oxide during the last 140 000 years, Earth Planet. Sc. Lett., 300, 33–43, 2010b. 5474, 5502, 5507

Schmidt, M. W. and Spero, H. J.: Meridional shifts in the marine ITCZ and the tropical hydrologic cycle over the last three glacial cycles, Paleoceanography, 26, PA1206, doi:10.1029/2010PA001976, 2011. 5489

Schwander, J., Barnola, J. M., Andrie, C., Leuenberger, M., Ludin, A., Raynaud, D., and Stauffer, B.: The age of the air in the firn and the ice at Summit, Greenland, J. Geophys. Res.-Atmos., 98, 2831–2838, 1993. 5480, 5481

Singarayer, J. S., Valdes, P. J., Friedlingstein, P., Nelson, S., and Beerling, D. J.: Late Holocene methane rise caused by orbitally controlled increase in tropical sources, Nature, 470, 82–85, 2011. 5486, 5490, 5508

Interpolar difference of atmospheric methane

M. Baumgartner et al.

Title Page

Abstract	Introduction
Conclusions	References
Tables	Figures

|◄ | ►|

◄ | ►

Back | Close

Full Screen / Esc

Printer-friendly Version

Interactive Discussion

Sowers, T.: Atmospheric methane isotope records covering the Holocene period, Quaternary Sci. Rev., 29, 213–221, 2010. 5484, 5488

Spahni, R., Schwander, J., Flückiger, J., Stauffer, B., Chappellaz, J., and Raynaud, D.: The attenuation of fast atmospheric CH_4 variations recorded in polar ice cores, Geophys. Res. Lett., 30, 1571, doi:10.1029/2003GL017093., 2003. 5480, 5481

Stager, J. C., Ryves, D. B., Chase, B. M., and Pausata, F. S. R.: Catastrophic drought in the Afro-Asian monsoon region during Heinrich Event 1, Science, 331, 1299–1302, 2011. 5488

Steele, L., Dlugokencky, E., Lang, P., Tans, P., Martin, R., and Masarie, K.: Slowing down of the global accumulation of atmospheric methane during the 1980s, Nature, 358, 313–316, 1992. 5483

Stenni, B., Buiron, D., Frezzotti, M., Albani, S., Barbante, C., Bard, E., Barnola, J. M., Baroni, M., Baumgartner, M., Bonazza, M., Capron, E., Castellano, E., Chappellaz, J., Delmonte, B., Falourd, S., Genoni, L., Iacumin, P., Jouzel, J., Kipfstuhl, S., Landais, A., Lemieux-Dudon, B., Maggi, V., Masson-Delmotte, V., Mazzola, C., Minster, B., Montagnat, M., Mulvaney, R., Narcisi, B., Oerter, H., Parrenin, F., Petit, J. R., Ritz, C., Scarchilli, C., Schilt, A., Schüpbach, S., Schwander, J., Selmo, E., Severi, M., Stocker, T. F., and Udisti, R.: Expression of the bipolar see-saw in Antarctic climate records during the last deglaciation, Nat. Geosci., 4, 46–49, 2011. 5479, 5502

Stocker, T. F. and Johnsen, S. J.: A minimum thermodynamic model for the bipolar seesaw, Paleoceanography, 18, doi:10.1029/2003PA000920, 920, 1087, 2003. 5473

Tans, P.: A note on isotopic ratios and the global atmospheric methane budget, Global Biogeochem. Cy., 11, 77–81, 1997. 5482

Wang, Y. J., Cheng, H., Edwards, R. L., An, Z. S., Wu, J. Y., Shen, C. C., and Dorale, J. A.: A high-resolution absolute-dated Late Pleistocene monsoon record from Hulu Cave, China, Science, 294, 2345–2348, 2001. 5484, 5488, 5507

Weber, S. L., Drury, A. J., Toonen, W. H. J., and van Weele, M.: Wetland methane emissions during the Last Glacial Maximum estimated from PMIP2 simulations: climate, vegetation, and geographic controls, J. Geophys. Res.-Atmos., 115, D06111, doi:10.1029/2009JD012110, 2010. 5473, 5486

Interpolar difference of atmospheric methane

M. Baumgartner et al.

Table 1. List of tie points for CH_4 synchronisation of NGRIP to unified EDML gas age scale (Lemieux-Dudon et al., 2010).

NGRIP depth (m)	EDML depth (m)	Gas age (yr BP)	Uncertainty (yr)
1481.2	692.2	11 067	50
1502.6	703.6	11 334	50
1514.7	711.2	11 490	50
1518.0	716.6	11 592	50
1519.7	724.0	11 707	50
1540.1	759.2	12 449	50
1553.2	772.0	12 835	50
1560.4	775.6	12 943	50
1580.2	791.5	13 397	50
1597.8	803.2	13 735	50
1627.5	823.7	14 367	50
1630.2	827.3	14 472	50
1641.2	835.7	14 705	50
1693.5	938.7	17 804	500
1762.8	995.2	20 414	200
1770.5	1005.9	20 889	50
1780.4	1014.0	21 218	50
1792.5	1031.2	21 872	50
1796.9	1037.1	22 112	50
1826.6	1067.0	23 097	50
1828.8	1071.0	23 237	50
1868.4	1139.2	26 956	50
1882.7	1146.7	27 261	200
1890.4	1151.9	27 579	50
1893.7	1159.7	28 091	50
1900.3	1169.0	28 561	50
1906.9	1171.7	28 699	50
1911.3	1174.0	28 833	50
1919.0	1181.9	29 240	50
1937.7	1195.6	30 031	50
1944.9	1207.6	30 771	200

Title Page

Abstract | Introduction

Conclusions | References

Tables | Figures

Back | Close

Full Screen / Esc

Printer-friendly Version

Interactive Discussion

Table 2. List of time intervals where the *IPD* is calculated (see also Fig. 1).

Interval		Mean Age (yr BP)	Duration (yr)	NGRIP (Points)[*]	CH$_4$ (ppbv)	Error (ppbv)	EDML (Points)	CH$_4$ (ppbv)	Error (ppbv)	*IPD* (ppbv)	Error (ppbv)	*rIPD* (%)	Error (%)	s_n (Tgyr^{-1})	s_s (Tgyr^{-1})	s_{tot} (Tgyr^{-1})
(I)	YD	12 078	742	21	506.9	1.8	22	479.5	3.2	27.4	3.9	5.6	0.8	93	49	142
(II)	BA1	13 339	792	34	686.0	4.2	13	642.5	4.0	43.5	6.5	6.6	1.0	130	61	191
(III)	BA2	14 044	617	29	655.0	3.1	11	612.1	4.3	42.9	5.5	6.8	0.9	126	57	182
(IV)	H1	16 254	3099	55	463.2	1.9	39	429.1	1.6	34.1	7.1	7.6	1.6	92	37	129
(V)[+]	St1	19 109	2611	63	395.9	1.2	29	372.5	1.3	23.4	2.0	6.1	0.5	74	37	111
(VI)	LGM	21 545	656	17	376.7	1.8	20	362.8	1.5	13.8	2.5	3.7	0.7	64	42	107
(VII)	DO2	22 605	984	35	419.0	1.8	28	390.2	1.1	28.9	2.1	7.1	0.5	81	35	117
(VIII)	St2	25 672	2568	34	387.2	2.1	49	368.2	1.4	19.0	3.1	5.0	0.8	70	39	109
(IX)	St2	27 108	306	14	408.3	2.9	11	386.7	1.9	21.6	4.0	5.4	1.0	75	40	114
(X)[°]	DO3	27 600	0	1	461.5	6.7	1	448.1	8.3	13.4	10.7	2.9	2.3	76	55	131
(XI)[°]	DO4	28 750	0	1	518.7	7.2	1	487.3	9.7	31.4	12.1	6.2	2.4	98	47	145
(XII)	St3	30 005	1531	32	421.9	2.4	21	394.3	2.2	27.5	3.8	6.7	0.9	81	37	118

[*] Due to the variation of the NGRIP tie points (Sect. 3.2), this is the mean value of all simulations and might thus not be an integer number.
[°] *IPD* estimate based on one point (maxima of DO event) and after application of the firn model.
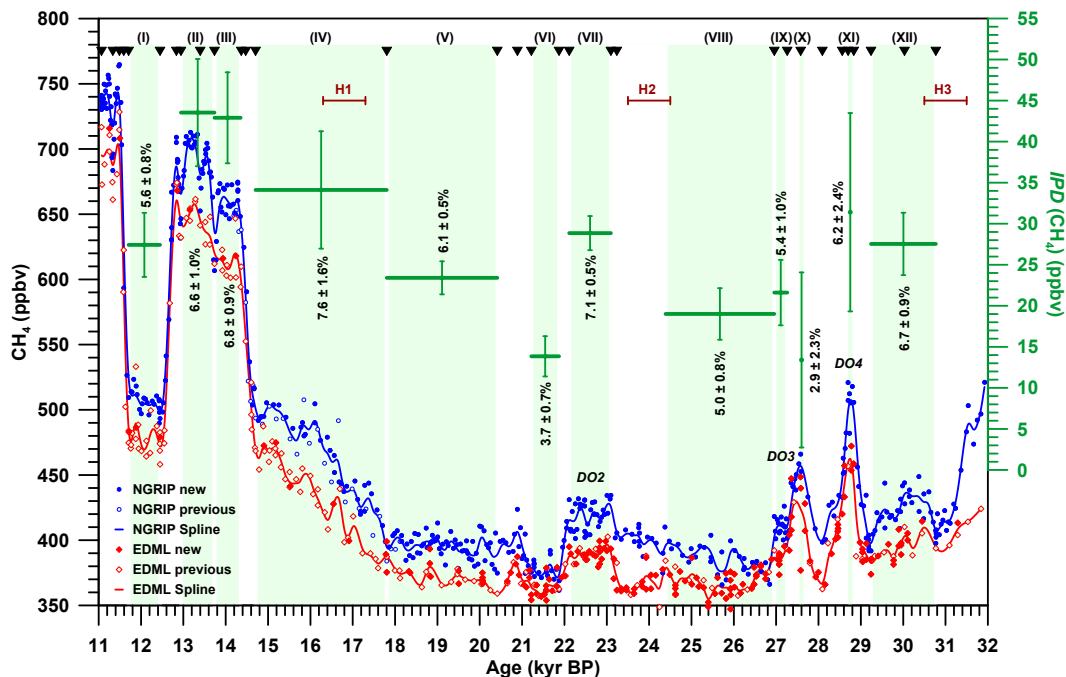[+] Used as reference interval in Fig. 6d.

Fig. 1. Atmospheric CH_4 concentration between 32 and 11 kyr BP reconstructed from polar ice core measurements. Data from Greenland (NGRIP) are plotted as blue circles and data from Antarctica (EDML) as red diamonds. Earlier published data (NGRIP from Schilt et al. (2010a) and EDML from EPICA Community Members (2006)) are shown as open symbols. The splines through the data are calculated according to Enting (1987) with a cutoff period of 350 yr. Mean *IPD* values (Table 2) are in green, where the horizontal bar and the green shaded area indicate the time interval and the vertical error bar shows the standard error of the mean. Corresponding relative *rIPD* values are indicated as black numbers. Heinrich Events (H) 1 to 3 (Hemming, 2004) are indicated in brown. Tie points for synchronisation (Sect. 2.1) are indicated on the top as black triangles. All CH_4 concentrations are synchronised to the unified EDML gas age scale derived by Lemieux-Dudon et al. (2010).

Title Page

Abstract | Introduction

Conclusions | References

Tables | Figures

|◄ | ►|

◄ | ►

Back | Close

Full Screen / Esc

Printer-friendly Version
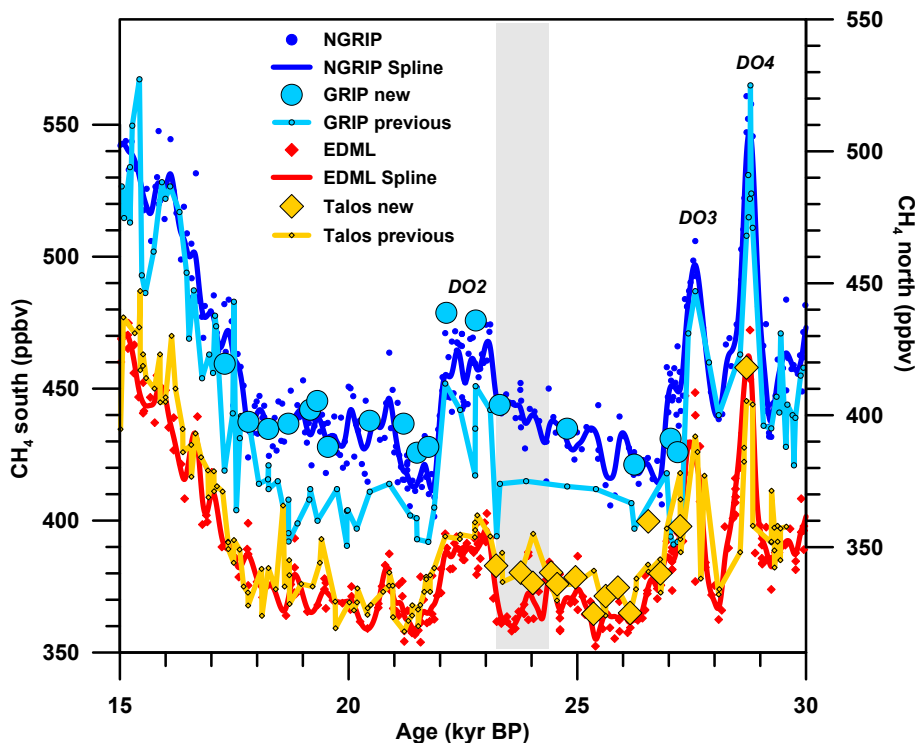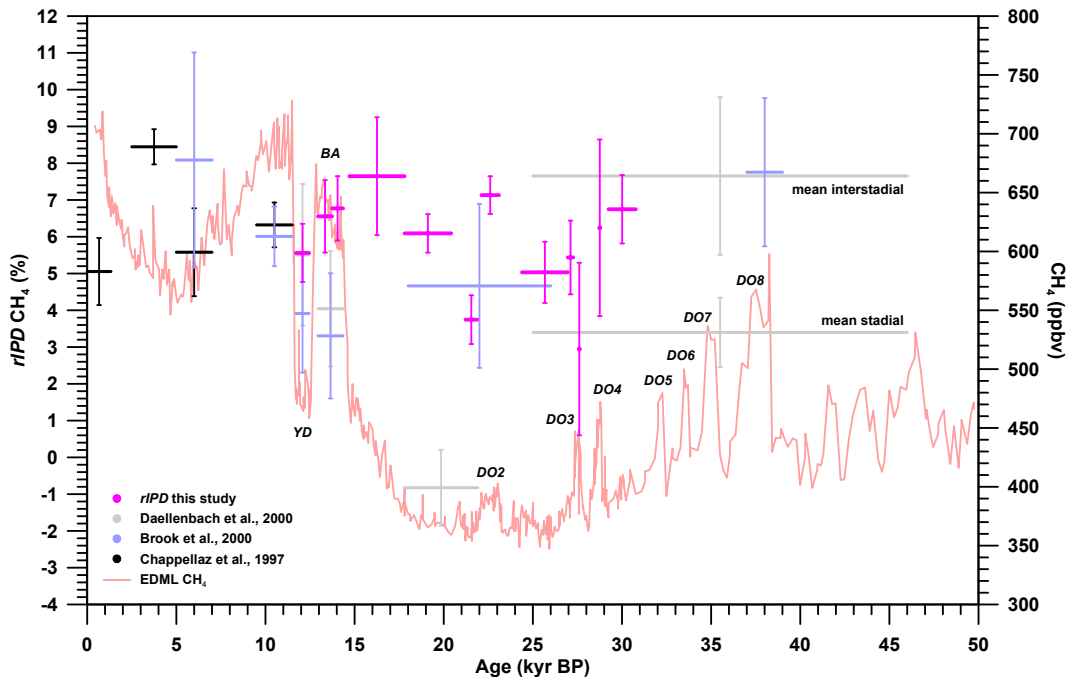
Interactive Discussion

Fig. 2. Remeasurements along the GRIP and TALDICE ice cores. For clarity reasons, data from Greenland (circles) and Antarctica (diamonds) are shown on different concentration axis. The NGRIP (blue, Schilt et al. (2010b) and new data) and EDML (red, EPICA Community Members (2006) and new data) data are the same as in Fig. 1. Additionally plotted are the previous GRIP record (Blunier et al., 1998; Dällenbach et al., 2000) (light blue) and the TALDICE record (Buiron et al., 2011; Stenni et al., 2011) (yellow). New GRIP and TALDICE remeasurements are shown as big light blue and yellow symbols, respectively. The grey shaded area marks the time interval, where the EDML record deviates from the TALDICE record. All CH_4 concentrations are synchronised to the unified EDML gas age scale derived by Lemieux-Dudon et al. (2010).

Fig. 3. Compilation of *rIPD* values for atmospheric CH$_4$ reconstructed from polar ice cores. Values from previous studies are given in black (Chappellaz et al. (1997): based on GRIP, D47 and Byrd) blue (Brook et al. (2000): based on GISP2 and Taylor Dome) and grey (Dällenbach et al. (2000): based on GRIP, Byrd and Vostok). New values, corresponding to the time intervals of Fig. 1 and Table 2, are shown in pink. The CH$_4$ concentration from EDML is plotted in red. All data are synchronised to the unified EDML gas age scale derived by Lemieux-Dudon et al. (2010).
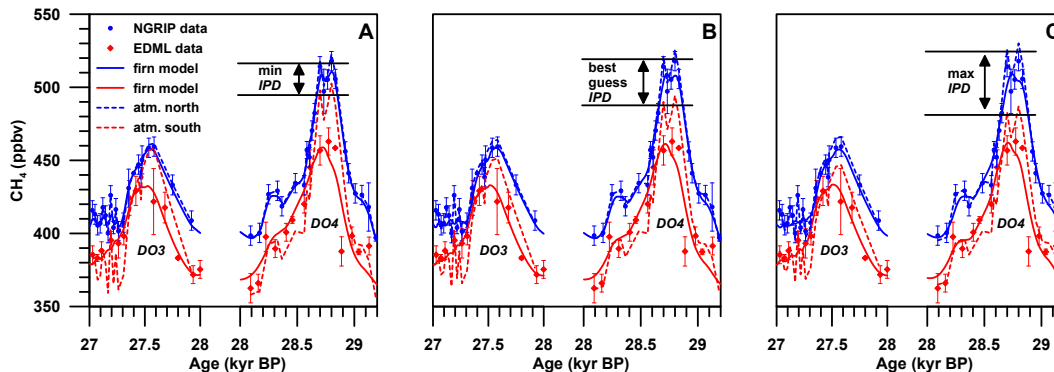
Fig. 4. Firn model applied on DO events 3 and 4. Shown are the NGRIP data (blue circles) and EDML data (red diamonds) corresponding to Fig. 1. Atmospheric signals constructed by linear scaling and shifting the NGRIP data are shown as dotted lines. The corresponding firn model output is shown in blue for NGRIP and in red for EDML. **(A)** Minimum *IPD*: Minimum attenuation at NGRIP, Maximum attenuation at EDML. **(B)** Mean *IPD*: Mean attenuation at NGRIP, Mean attenuation at EDML. **(C)** Maximum *IPD*: Maximum attenuation at NGRIP, Minimum attenuation at EDML.

Title Page

Abstract | Introduction

Conclusions | References

Tables | Figures

◄ | ►

◄ | ►

Back | Close

Full Screen / Esc

Printer-friendly Version

Interactive Discussion

Interpolar difference of atmospheric methane
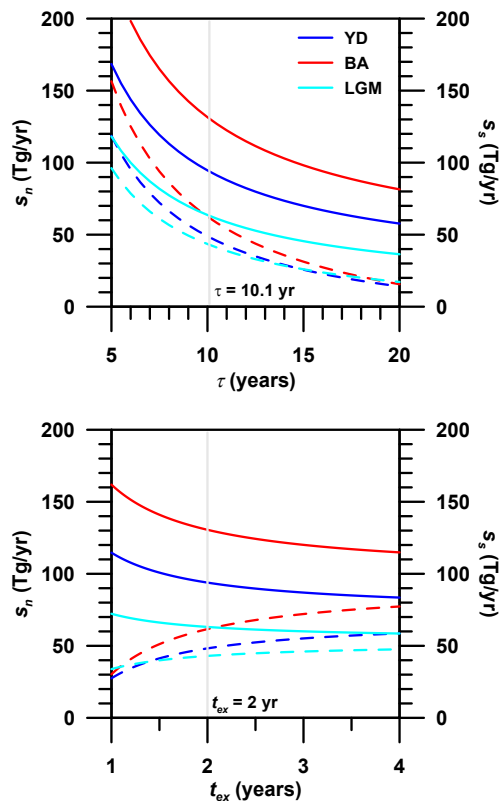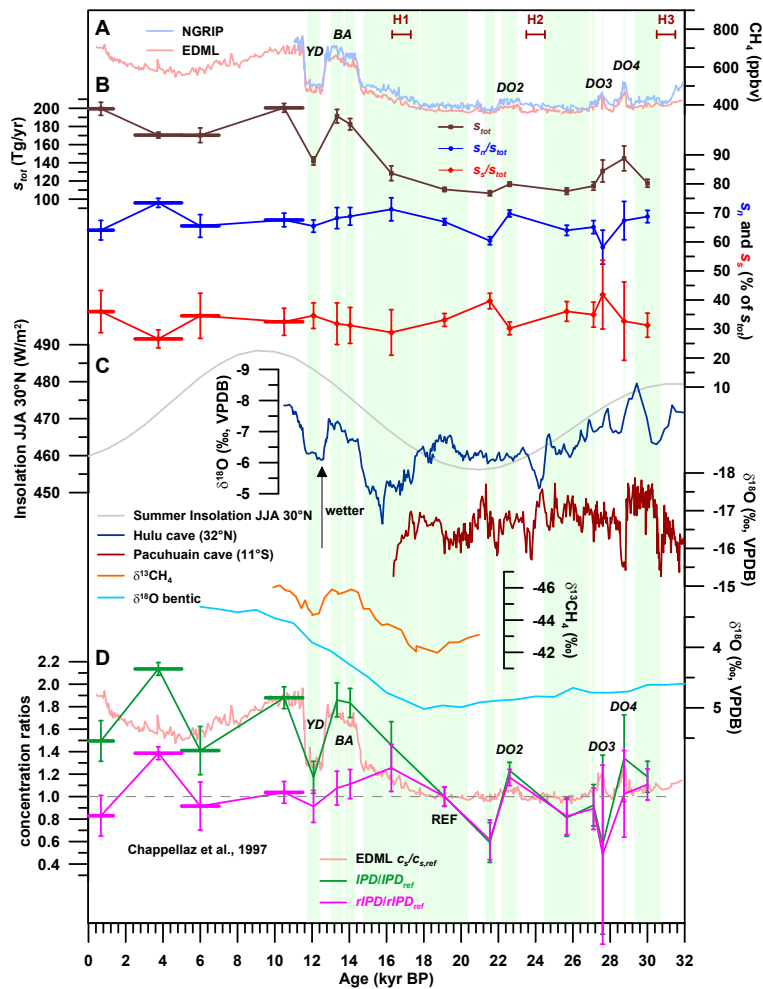
M. Baumgartner et al.

Fig. 5. Sensitivity of CH_4 sources to τ and t_{ex}. Source distribution (solid lines: s_n, dashed lines: s_s) calculated for three different climate states (blue: YD, red: BA, light blue: LGM; concentrations from Table 2) depending on τ (upper panel) and t_{ex} (lower panel). While one parameter is varied, the other is set to $\tau = 10.1$ yr and $t_{ex} = 2$ yr (grey lines), respectively, according to the initialisation with today's source distribution from Fung et al. (1991).

Fig. 6. Caption on next page.

Title Page

Abstract | Introduction

Conclusions | References

Tables | Figures

|◄ | ►|

◄ | ►

Back | Close

Full Screen / Esc

Printer-friendly Version

Interactive Discussion

Fig. 6. Variations in the CH_4 source strength. Green shaded areas are the same as in Fig. 1 and indicate the time interval, wherein each point is the mean value of its time interval (Table 2). On the left side, the four Holocene values from Chappellaz et al. (1997) are also included, where the horizontal bars indicate the time interval. **(A)** CH_4 concentrations from EDML (red, EPICA Community Members, 2006, and new data) and NGRIP (blue, Schilt et al., 2010b, and new data). **(B)** Source strengths estimated by the two-box model. Brown: total source strength, Blue: northern source strength as a fraction of s_{tot}, Red: southern source strength as a fraction of s_{tot}. **(C)** Grey: Northern summer insolation (30° N) (Quinn et al., 1991), Dark blue: monsoon record from Hulu Cave (Wang et al., 2001), Dark red: monsoon record from Pacupahuain cave (Kanner et al., 2012), Orange: $\delta^{13}CH_4$ (Fischer et al., 2008), Light blue: benthic $\delta^{18}O$ (Lisiecki and Raymo, 2005). **(D)** Red: ratio $c_s/c_{s,ref}$ (from EDML, (EPICA Community Members, 2006) and new data), Green: ratio IPD/IPD_{ref} (Chappellaz et al., 1997, and new data), Pink: ratio $rIPD/rIPD_{ref}$ (Chappellaz et al., 1997, and new data). Interval (V) from Table 2 is used as the reference interval, to put all the ratios on the same scale.

With the exception of the benthic $\delta^{18}O$ and the monsoon records, which are shown on their original time scales, all data are synchronised to the unified EDML gas age scale derived by Lemieux-Dudon et al. (2010).
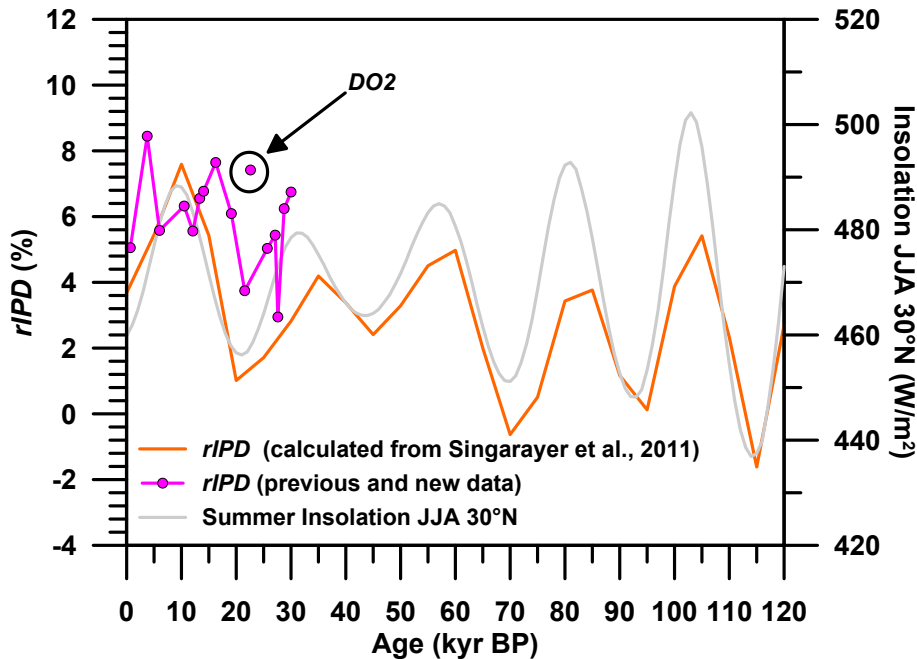
Fig. 7. *rIPD* long-term trend estimated from the CH$_4$ source distribution by Singarayer et al. (2011). The *rIPD* (orange) was calculated according to Eqs. (8) and (9). Measured *rIPD* data (Brook et al., 2000; Chappellaz et al., 1997, and new data) are shown in pink. Northern summer insolation (JJA) (30° N) is plotted in grey (Quinn et al., 1991).

Title Page

Abstract | Introduction

Conclusions | References

Tables | Figures

◄ | ►

◄ | ►

Back | Close

Full Screen / Esc

Printer-friendly Version

Interactive Discussion